PCCP

ROYAL SOCIETY OF CHEMISTRY

PAPER

View Article Online
View Journal | View Issue

Check for updates

Cite this: *Phys. Chem. Chem. Phys.*, 2025, **27**, 5198

Effects of doping on anti-phase boundaries and the magnetic properties of the $D0_3$ structure in high silicon steel: first-principles insights†

Meng Sun,[a] Linxian Li,[a] Hongyu Song,[a] Shuai Tang, *[a] Qing Peng, *[b] Guichang Shen,[a] Tianwei Xie,[c] Fengliang Tan[d] and Zhenyu Liu[a]

Received 31st October 2024,
Accepted 3rd February 2025

DOI: 10.1039/d4cp04178j

rsc.li/pccp

The $D0_3$ ordered structure is crucial for the room-temperature plasticity of high silicon steel. The formation of anti-phase boundaries (APBs) due to dislocation movement in the ordered structures hinders subsequent dislocation motion, leading to embrittlement. A low anti-phase boundary energy (γ_{APB}) can facilitate dislocation slip and enhance the plastic deformation capability of the ordered structures. In this study, we calculated γ_{APB} of two types of APBs of $D0_3$ (110) ⟨111⟩ by substituting Fe atoms with six transition metals: Ti, V, Cr, Zr, Nb, and Mo. We also evaluated the mechanical constants and magnetic moments of the doped $D0_3$ structures. The results show that doping Cr, Nb, and Mo significantly reduces γ_{APB}, positively affecting the plasticity of $D0_3$. Charge density analysis indicates that Cr, Nb, and Mo, particularly Cr and Mo, increase charge transfer between atoms across the APBs, enhancing interatomic interactions. This gives a new theoretical explanation for the experimental findings that Cr and Nb can improve the plasticity of high silicon steel. Additionally, alloying elements influence the total magnetic moment of $D0_3$ compounds by altering the local environment of Fe atoms closest to Si, interatomic interactions, and the unpaired electrons in the d-band of the compounds.

1. Introduction

Silicon steel is applied in electric machines, generators, transformers, and reactors because of its superior soft magnetic properties, such as high permeability, high resistivity, and low iron loss.[1] The soft magnetic properties of silicon steel improve with an increase in the Si content. The material exhibits exceptionally good soft magnetic properties when the Si content reaches 6.5 wt% (namely high silicon steel),[2,3] with a significant increase in magnetic permeability, a near-zero magnetostriction coefficient, and a considerable reduction in iron loss. However, high Si content greatly increases material brittleness. High silicon steel has almost zero room-temperature plasticity, making it difficult to machine, process, and reshape.[4,5]

The B2 and $D0_3$ ordered phases in the matrix significantly contribute to the severe brittleness of high silicon steel at room temperature.[6,7] Dislocations in the ordered phases possess higher energy,[8] making them difficult to move, resulting in poor plastic deformation ability. The order degree of the matrix can be reduced through process measures. During warm rolling, the motion of super dislocations continuously disrupts and fragments the ordered phases resulting in gradually reducing their size and number.[9] Raviprasad[10] found that rapid cooling prevents Fe and Si from timely rearranging, inhibiting the $D0_3$ ordered phase formation. However, the critical Si content for inhibiting the B2 ordered phase formation is 5.87 wt%.[11] Hence, completely preventing ordered phase formation through rapid cooling in high silicon steel is hard. Many researchers have conducted extensive studies on controlling the order degree of the matrix through alloying. Chen[12] found that after adding 1 wt% Cr to 6.5 wt% Si steel, the relative intensity of superlattice spots of ordered phases decreased from 1.0 in the sample without Cr to 0.784, indicating a reduction in the number of ordered phases. Yu[13] observed in experiments that the addition of Ni led to a reduction in both the B2 and $D0_3$ phase content in the matrix. Lin[14] discovered that compared to samples without Nb, under conditions of 800 °C/0.01 s thermal deformation, the size of B2 decreased in a 0.15 wt% Nb sample, and $D0_3$ can not be observed. Cheng *et al.*[15,16] found that adding 0.5 wt% Cu reduced the long-range order in the matrix of high silicon steel, leading to an improvement in plasticity. Various process

[a] State Key Laboratory of Rolling and Automation, Northeastern University, Shenyang 110819, China. E-mail: tangshuai@ral.neu.edu.cn
[b] State Key Laboratory of Nonlinear Mechanics, Institute of Mechanics, Chinese Academy of Sciences, Beijing 100190, China. E-mail: pengqing@imech.ac.cn
[c] Beijing Shougang Company Limited, Shougang Group, Qianan 064400, China
[d] School of Materials and Environmental Engineering, Hunan University of Humanities Science and Technology, Loudi 417000, Hubei, China

† Electronic supplementary information (ESI) available. CCDC 2420807, 2420810 and 2420813. For ESI and crystallographic data in CIF or other electronic format see: https://doi.org/10.1039/d4cp04178j

methods and the addition of alloy elements can improve matrix plasticity. The plastic deformation ability of ordered structures in the matrix can be improved by reducing the resistance of dislocation sliding.

After sliding in the ordered structure, dislocations disrupt the ordered arrangement of atoms, and a mismatch interface known as an anti-phase boundary (APB) between the sliding and non-sliding atoms is generated.[17] The anti-phase boundary energies (γ_{APB}) are the energy barrier that dislocations have to overcome to continue sliding at the APB. Dislocations are prone to gather at APBs and cause dislocation pile-ups.[18,19] The magnitude of γ_{APB} influences the difficulty of dislocation slip in ordered alloys,[20] and a small γ_{APB} is conducive to promoting the independent movement of dislocations.[20,21] Therefore, reducing γ_{APB} is beneficial for the plastic deformation of ordered structures. There is extensive research on the effect of alloying element doping on γ_{APB}. Li[22] calculated γ_{APB} of intermetallic compounds after doping with different alloying elements and found that different alloying elements have varying effects on different intermetallic compounds. Yoshimi[18] discovered that under the same strain conditions, adding Cr to the Fe–28Al alloy reduced γ_{APB} of the $D0_3$ structure from 66 mJ m^{-2} to 49 mJ m^{-2}. Cheng[23] studied the substitution behavior of Cu in the $D0_3$ compound based on the observed improvement of matrix plasticity experimentally.[15,16] The computational results indicated that when Cu occupied Fe sites, the $D0_3$ compound exhibited enhanced plasticity and decreased γ_{APB}. Sundar[24] observed the segregation of V at APB in Fe–Co alloys in experiments. Li[21,25] further confirmed through first-principles calculations that V can reduce γ_{APB} of the (110) and (112) planes of the B2 structure in Fe–Co alloys. While alloying elements affect γ_{APB}, they also change the magnetic moment of the compounds. Mao[26] studied the impact of adding Mn and In (indium) on the magnetic moment of Sm (samarium)–Co alloys through first-principles calculations. The total magnetic moment of the compounds increased after adding Mn and decreased after adding In, suggesting that various dopants produce distinct impacts on the total magnetic moment of the compounds. However, there is currently limited research on how alloying elements influence APBs in the ordered structures in high silicon steel. Meanwhile, the influence of alloying elements on the magnetic moment of ordered structures must be considered.

Based on previous studies on the effects of alloying elements on ordered structures in high silicon steel and the impact on the APBs in the B2 and $D0_3$ ordered structures in different alloy systems, this paper investigates the effects of six transition metal elements Ti, V, Cr, Zr, Nb, and Mo on two types of APBs of (110) ⟨111⟩, mechanical constants, and magnetic moments of $D0_3$. The mechanism of the elements that affect APBs and the magnetic moment of $D0_3$ is revealed from an electronic perspective.

2. Theoretical methods

In high silicon steel, the matrix primarily comprises the A2 disordered structure, along with B2 and $D0_3$ ordered structures. Disordered structures exhibit random atomic arrangements, whereas ordered structures display periodicity. The densely packed plane of the $D0_3$ ordered structure is (110), with the dense packing direction of ⟨111⟩. The perfect dislocations in the ordered structure independently slip difficultly. Thus, they decompose into four partial dislocations (b_1, b_2, b_3, and b_4), with three APBs (NNAPB, NNNAPB, and NNAPB) connecting in between. Among these, the displacement of partial dislocations b_1 and b_4 leads to the NNAPB and is related to the misplacement of the nearest neighbor atoms. The displacement of the middle two partial dislocations, b_2 and b_3, results in the NNNAPB and is related to the misplacement of the next nearest neighbor atoms.[27,28] Here, the NNAPB is abbreviated as APB_I, and the NNNAPB is abbreviated as APB_{II}. The slip modes of partial dislocations b_1 and b_2 of the $D0_3$ (110) plane are illustrated in Fig. 1(a1) and (b1), respectively. After slip of partial dislocations, there is a rearrangement of atoms, leading to the formation of new crystal planes as shown in Fig. 1(a2) and (b2). Periodic boundary conditions are applied in all the three orthogonal directions. The size of the simulation box is

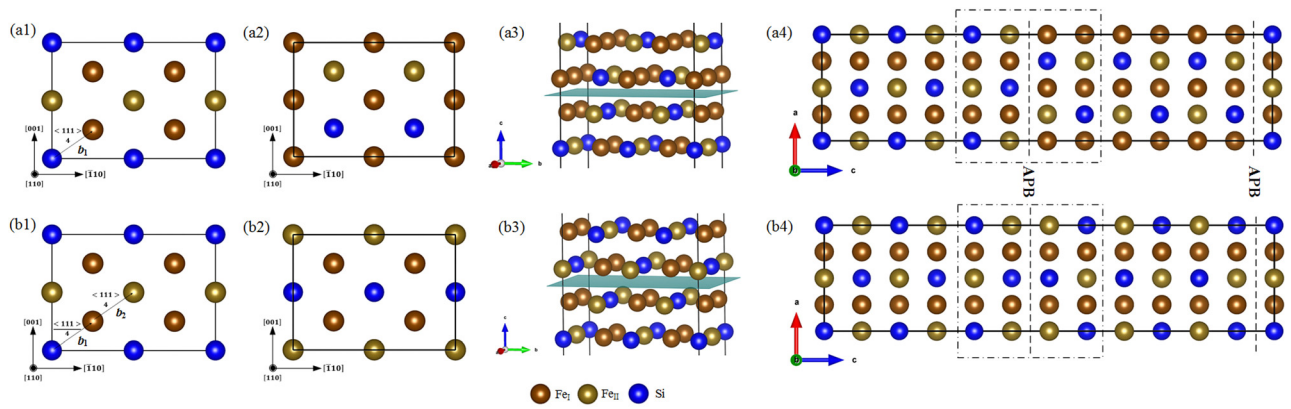

Fig. 1 Slip modes of partial dislocations b_1 and b_2 and APB models. (a1) Schematic diagram of partial dislocation b_1 slip on the (110) plane; (a2) schematic diagram of atomic arrangement after partial dislocation b_1 slip, the atomic layer above the blue plane in (a3); (a3) magnified view of APB_I within the dashed box in (a4); (a4) APB_I model. (b1) Schematic diagram of partial dislocation b_2 slip on the (110) plane; (b2) schematic diagram of atomic arrangement after partial dislocation b_2 slip, the atomic layer above the blue plane in (b3); and (b3) magnified view of APB_{II} within the dashed box in (b4); (b4) APB_{II} model.

well chosen to compromise the accuracy of γ_{APB} and avoid APB–APB interactions and maximize computational cost. There are two models to calculate γ_{APB} of APB_I (γ_{APBI}) and APB_{II} (γ_{APBII}). According to the tests, when the number of layers ranged from 6 to 16, the maximum variation in $\Delta\gamma_{APB}$ did not exceed 30 mJ m^{-2}, consistent with the results reported by William.[29] To ensure accuracy while optimizing computational efficiency, we ultimately selected a supercell with 12 atomic layers, containing a total of 96 atoms. Additionally, we used the same model to calculate the anti-phase boundary energy of the B2 structure in Fe–Co alloys, and the calculated value is 119 mJ m^{-2}. The calculated value by Li *et al.* is 126 mJ m^{-2}.[21,25] The small error in our results further validates the reliability of the model. Therefore, the models with 12 atomic layers and a total of 96 atoms were adopted, as illustrated in Fig. 1(a4) and (b4), with a magnified view presented in Fig. 1(a3) and (b3).

The calculation adopted the density functional theory (DFT) quantum mechanics first-principles calculation method and is carried out using the Vienna Ab initio Simulation Package (VASP).[30,31] Exchange–correlation potentials between electrons were parameterized by the generalized gradient approximation (GGA)[32] with the Perdew–Burke–Ernzerhof (PBE)[33] function. The energy convergence criterion was 10^{-5} eV per atom for electronic relaxation. Structural relaxation was conducted using the conjugate gradient method, with a convergence criterion of all interatomic forces below 0.03 eV $Å^{-1}$. Cutoff energy and *K*-point convergence calculations were conducted on the $D0_3$ unit cell. It was found that when the cutoff energy was set as 400 eV and the *K*-point was set as $6 \times 6 \times 6$, the total energy fluctuation was very small (less than 1.5 meV per atom). The experimental value[34] of the lattice constant is 5.65 Å, and our calculated value is 5.60 Å, with an error of less than 1%. On this basis, the anti-phase boundary models were built and *K*-point testing was conducted. When the *K*-point was set as $6 \times 4 \times 1$, the total energy fluctuation was less than 1 meV per atom. When determining the atomic occupied sites and calculating the mechanical constants and magnetic moment, a model containing 16 atoms was used (Fig. 2). After optimized calculations, the bulks were fixed, and atomic positions were allowed to relax. Research studies indicate that the $D0_3$ structure exhibits a ferromagnetic behavior.[35,36] During the magnetic ground state testing of the system, the total energy of the system was calculated for both ferromagnetic (FM) and antiferromagnetic (NM) states. The calculation results indicate that the total energy is lower when the system is in a ferromagnetic state. When in an antiferromagnetic state, it is the opposite. Therefore, the system is in a ferromagnetic state. So spin polarization was considered to characterize the magnetism. The crystal and electronic structures were visualized by VESTA.[37,38]

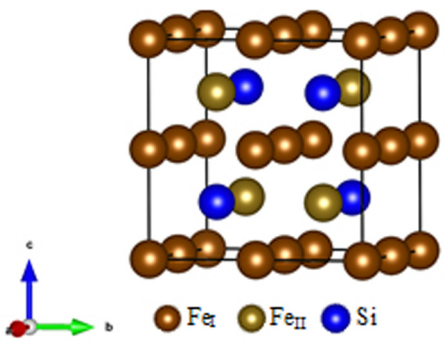

Fig. 2 Fe_I, Fe_{II}, and Si sites in the $D0_3$ structure.

3. Results and discussion

3.1. Anti-phase boundary energies

Firstly, the sites where solute atoms were occupied in the $D0_3$ structure were determined. There are three types of sites: Fe_I, Fe_{II}, and Si, each with 8, 4, and 4, as shown in Fig. 2.

The Fe_I sites are closest to the Si sites, followed by the Fe_{II} sites. The sites of solute atoms occupied in the lattice are determined using eqn (1).[21,25]

$$\Delta E_M = \min\left\{E_M^{Fe_I}, E_M^{Fe_{II}}\right\} + \mu_{Fe} - \mu_{Si} + E_M^{Si} \quad (1)$$

where $E_M^{Fe_I}$, $E_M^{Fe_{II}}$, and E_M^{Si} represent the total energy of the supercell with solute atoms occupying the Fe_I, Fe_{II}, and Si sublattice sites, respectively. μ_{Fe} and μ_{Si} are the chemical potentials of Fe and Si atoms in $D0_3$. A smaller ΔE_M indicates a stronger tendency for solute atoms to occupy that site. Ni and Cu were also considered in reference to previous research. The selective occupancy of transition metals in the $D0_3$ lattice correlates with their position in the periodic table. Elements positioned to the right of Fe in the periodic table (Co, Ni, and Cu) preferentially occupy the Fe_I site, whereas those positioned to the left of Fe (Ti, V, Cr, and Mn) preferentially occupy the Fe_{II} site.[39–42] The calculation results also follow this pattern, with Cu and Ni located on the right side of Fe preferentially occupying the Fe_I site, while Ti, V, Cr, Zr, Nb, and Mo elements located on the left side of Fe preferentially occupying the Fe_{II} site.

We used *ab initio* molecular dynamics (AIMD) simulations to evaluate the thermal stability of two undoped anti-phase boundary models at four different temperatures (300 K, 500 K, 700 K, and 900 K). The calculation results are provided in the ESI.† The results indicate that both anti-phase boundaries have good thermal stability at high temperatures. To investigate the effect of solute atoms on the γ_{APB}, by introducing solute atoms at the APBs for analysis, γ_{APB} can be calculated using eqn (2).[19,29]

$$\gamma_{APB} = \frac{E_{APB} - E_0}{2A} \quad (2)$$

where E_{APB} is the total energy of the supercell with APB, E_0 is the total energy of the supercell without APB, and A represents the cross-sectional area of the APB. γ_{APBI} and γ_{APBII} are 456 mJ m^{-2} and 242 mJ m^{-2}, respectively. The value of γ_{APBI} is close to that reported in ref. 23 The partial dislocation b_1 completely changes the nearest neighbor relationship between Fe and Si atoms, while the partial dislocation b_2 only changes the nearest neighbor relationship of some atoms.[43] Correspondingly, γ_{APBI} is greater than γ_{APBII}, so as the calculation results. Fig. 3 shows the calculation results after introducing solute atoms at APBs, where

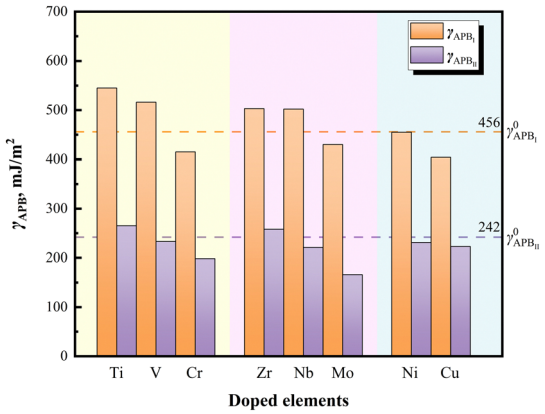

Fig. 3 γ_{APB} after alloying element doping.

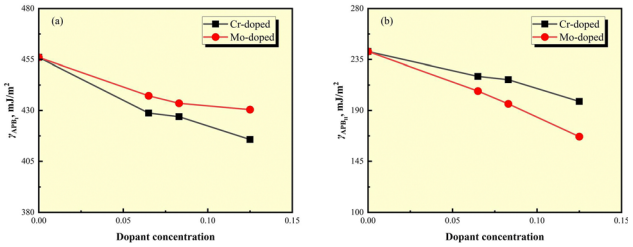

Fig. 4 γ_{APB} after Cr and Mo doping at different dopant concentrations, (a) γ_{APBI} after doping; (b) γ_{APBII} after doping.

γ^0_{APBI} and γ^0_{APBII} are the anti-phase boundary energies of APB_I and APB_{II} before doping, respectively. The results indicate that after alloying element doping, γ_{APB} gradually decreases as the alloying elements are arranged from left to right in the same period. APB_{II} is more sensitive to dopant elements than APB_I, and most dopant atoms reduce γ_{APBII}. While γ_{APBI} only can be reduced by the doping elements closest to Fe in the periodic table. The finding that doping Cr and Nb reduces γ_{APB} provides a new explanation for the mechanism of their effect on the plasticity of high silicon steel previously discovered.[12,14] Theoretically, adding Mo will also have a similar effect.

To investigate the effect of doping concentration on γ_{APB}, we changed the size of the supercell to alter the surface concentration of doping. Calculations were performed at lower doping concentrations after doping with Cr and Mo. The calculation results are shown in Fig. 4. With the increase of the doping surface concentration, γ_{APBI} (Fig. 4(a)) and γ_{APBII} (Fig. 4(b)) gradually decrease. This indicates that increasing the doping concentration of elements is beneficial for reducing γ_{APB}.

3.2. Mechanical properties

The elastic constants of various compounds of the doped $D0_3$ compounds were calculated and the results are shown in Table 1.

The elastic matrix comprises three constants, C_{11}, C_{12}, and C_{44} based on the symmetry of the cubic structures.[44] Born's criterion[45] can be used to determine the stability of the BCC structure through eqn (3). The calculation results indicate that both the $D0_3$ crystal structure and its doping variants satisfy mechanical stability.

Table 1 Elastic constants of $D0_3$ and compounds doped with alloying elements

Compounds	C_{11} (GPa)	C_{12} (GPa)	C_{44} (GPa)	B (GPa)	G (GPa)	E (GPa)
$D0_3$	285.51	181.67	143.80	216.28	107.05	275.67
Ti-doped	289.61	140.58	148.93	190.26	119.16	295.75
V-doped	315.21	175.28	142.32	221.92	113.38	290.64
Cr-doped	292.88	177.06	140.22	215.67	107.30	276.11
Zr-doped	353.96	181.20	150.32	238.79	124.74	318.73
Nb-doped	360.64	192.73	147.87	248.70	122.30	315.24
Mo-doped	353.92	198.57	140.39	250.36	115.31	299.88
Ni-doped	287.56	186.38	142.55	220.19	105.76	273.49
Cu-doped	274.44	192.02	144.60	219.50	103.25	267.76

$$C_{11} - |C_{12}| > 0, \quad C_{11} + 2C_{12} > 0, \quad C_{44} > 0 \tag{3}$$

Using Voigt's method,[46] we calculated the bulk modulus (B) [eqn (4)], shear modulus (G) [eqn (5)], and Young's modulus (E) [eqn (6)].

$$B = \frac{C_{11} + 2C_{12}}{3} \tag{4}$$

$$G = \frac{C_{11} - C_{12} + 3C_{44}}{5} \tag{5}$$

$$E = \frac{9BG}{G + 3B} \tag{6}$$

C_{11} represents the resistance to compressive deformation, and C_{44} represents the resistance to shear deformation. All structures exhibit C_{11} values greater than C_{44}, indicating a tendency for shear deformation to occur more readily. After doping with Ti, V, Cr, Zr, Nb, and Mo, the compounds exhibit lower C_{11} values compared to those of the undoped case, making them more susceptible to shear deformation. Furthermore, the increase in shear modulus (G) and Young's modulus (E) signifies increased material hardness. Given that the bulk modulus (B) indicates resistance to volume change under pressure, a higher B value signifies stronger atomic bonds, contributing to increased material strength. Therefore, the change in B values suggests that the lattice distortion from substituting Fe atoms with all atoms except Ti and Cr improves resistance to volume change under pressure, leading to higher material strength.

Pugh's criterion[47] states that the B/G ratio signifies whether a material exhibits ductility or brittleness. $B/G > 1.75$ signifies ductility, while a lower ratio indicates brittleness. The Cauchy pressure parameter (C_{12}–C_{44}) could be used to describe the plasticity of metallic materials. A larger Cauchy pressure parameter value indicates better plasticity. Fig. 5 presents the B/G value (a) and the Cauchy pressure parameter (b) of each compound. As the atomic number of doped elements in the same period increases, the B/G and Cauchy pressure parameter values of the doped compound also gradually increase. After doping with Nb and Mo, the B/G values increased by 0.49% and 7.5%, respectively, suggesting that they can improve the ductility of the material. Similarly, the Cauchy pressure parameter

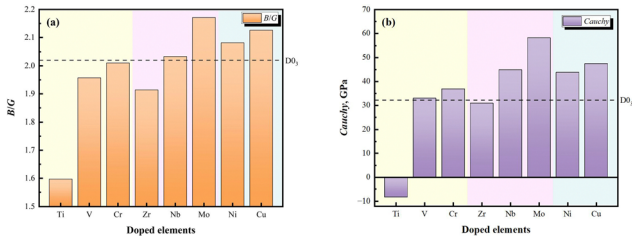

Fig. 5 (a) Calculated bulk to shear modulus ratio value (B/G); (b) Cauchy pressure parameter value ($C_{12}-C_{44}$).

value follows the same trend from left to right. After doping V, Cr, Nb, and Mo, the Cauchy pressure parameter value of the compounds increases significantly, indicating an improvement in the plastic deformation capability of the structure.

These calculation results indicate that the substation of Fe with dopants like Cr, Nb, and Mo elements improves the plasticity of $D0_3$.

3.3. Magnetic moments

The doping elements not only affect γ_{APB} of the ordered structure but also lead to changes in the magnetic moment.

Table 2 lists the local magnetic moment of each atom and the total magnetic moment of each compound.

When alloying elements are introduced, the local magnetic moment of Fe_I is significantly affected. The greater the influence on the local magnetic moment of Fe_I in a compound, the greater the impact on the total magnetic moment of the compound. Pugaczowa-Michalska[48] found that the main reason for the decrease in the total magnetic moment of $Fe_{3-x}Cr_xSi$ with increasing Cr concentration is the reduction in the local magnetic moment of Fe_I, unrelated to the changes in the local magnetic moment of Cr. The local magnetic moment of iron depends on their occupied sites in the crystal cell and the nearest neighbor configuration.[49] The nearest neighbor atoms of Fe_{II} sites are all Fe, with the local environment dominated by Fe atoms. The nearest neighbor atoms of Fe_I sites consist of Si and Fe. When doping atoms enter the lattice, the local environment of Fe_I atoms changes more significantly compared to that of Fe_{II}, resulting in a greater impact on their local magnetic moment. The effect of doping elements on the interactions between atoms can also alter the total magnetic moment of the system.[49,50] However, it should be noted that theoretical calculations may differ from reality due to model differences and the inability to capture all complex electron interactions that affect magnetic moments fully.

Table 2 Total magnetic moment of each compound and the local magnetic moment of Fe and doped atoms

Compounds	M_{Fe_I} (μ_B per atom)	$M_{Fe_{II}}$ (μ_B per atom)	M_m (μ_B per atom)	M_s (μ_B per cell)
$D0_3$	1.308	2.556	—	20.488
Ti-doped	0.781	2.590	−0.307	13.600
V-doped	0.850	2.631	−0.464	14.120
Cr-doped	0.864	2.642	−0.066	14.640
Zr-doped	0.628	2.541	−0.149	12.423
Nb-doped	0.734	2.608	−0.195	13.411
Mo-doped	0.799	2.611	−0.255	14.022
Ni-doped	1.216	2.587	0.336	19.042
Cu-doped	1.11	2.557	0.006	18.282

3.4. Electronic properties

3.4.1. Density of states. Fig. 6 shows the total density of states (TDOS) of each compound and the partial density of states (PDOS) of each atom. Among all compounds, the s-orbitals of Si atoms mainly contributed in the low energy region (from −12 eV to −7 eV). The TDOS of all compounds is contributed by the d-orbitals of Fe atoms and doped atoms from −7 eV to 3 eV, as well as the p-orbitals of Si atoms. After doping with alloy atoms, the TDOS of the compounds shifts towards a lower energy region, enhancing the stability of the compounds. Fe and doped atoms are both transition metals, and their d-orbital electrons significantly impact the total magnetic properties of the material.[48] Doped elements of the same period, such as Ti, V, Cr, Ni, and Cu, exhibit increasingly strong peaks in the d-orbitals of their PDOS. At the same time, the total magnetic moment of the compounds

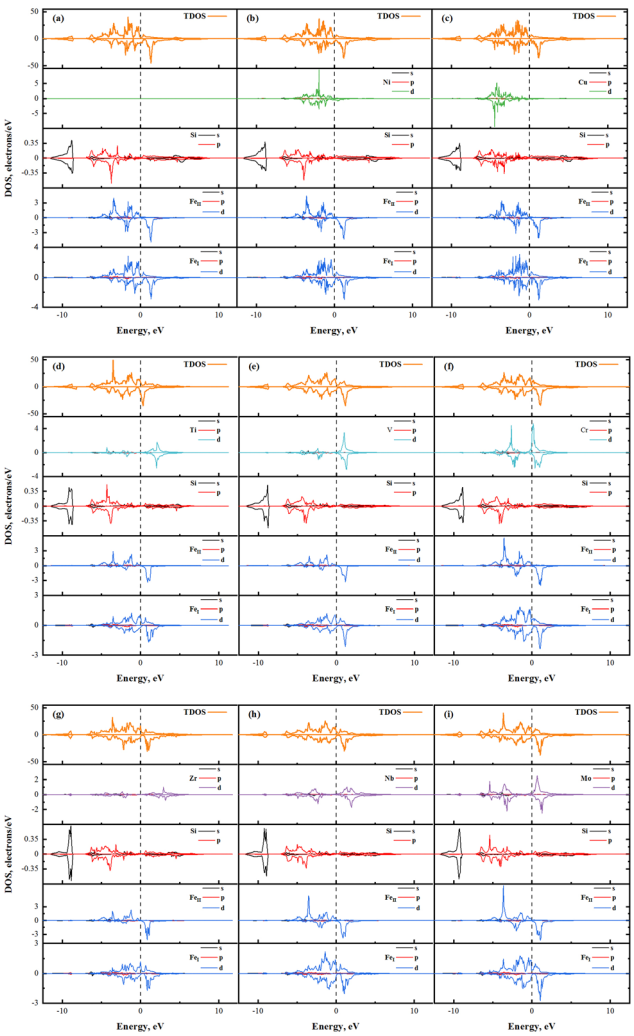

Fig. 6 TDOS and PDOS. (a) Undoped; (b) Ni-doped; (c) Cu-doped; (d) Ti-doped; (e) V-doped; (f) Cr-doped; (g) Zr-doped; (h) Nb-doped; and (i) Mo-doped.

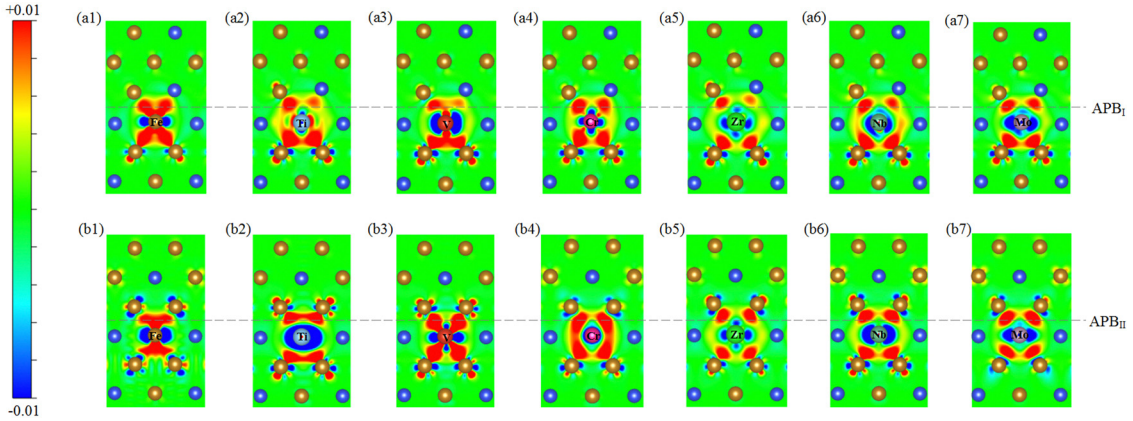

Fig. 7 Differential charge density maps of APBs, (a1) without doping at APB_I; (a2)–(a7) doped with Ti, V, Cr, Zr, Nb, and Mo at APB_I. (b1) Without doping at APB_{II}; (b2)–(b7) doped with Ti, V, Cr, Zr, Nb, and Mo at APB_{II}.

doped with them is less and less affected. The same applies to doped elements Zr, Nb, and Mo in the same period. This is because the electrons in the d-band of the compound have a significant impact on its total magnetic moment. The more unpaired electrons in the d-orbitals of the alloying atom, the more unpaired electrons are introduced into the d-band of the compound after doping. Thus, the greater impact on the total magnetic moment of compounds.

3.4.2. Charge density difference. The charge density difference maps of the APBs after Ti, V, Cr, Zr, Nb, and Mo doping are shown in Fig. 7. The blue color indicates electron consumption, while the red color signifies electron accumulation. The dashed lines represent APBs. To reflect the changes in charge transfer at the APBs after doping, the case without doping was also plotted. As shown in Fig. 7, regardless of doping or not, the atoms above the dashed lines (APBs) exhibit a decrease in charge transfer compared to the atoms below. This means that there are differences in the interactions between the atoms across APBs, and the interactions between the atoms above are weaker. Smaller γ_{APB} indicates enhanced APB strength,[25,29] and the interactions between the atoms above and below the dashed lines in APB_{II} (Fig. 7(b1)–(b7)) are stronger than those in APB_I (Fig. 7(a1)–(a7)). Therefore, γ_{APBII} is smaller and APB_{II} is stronger. In APB_I (Fig. 7(a2)–(a4)), the charge transfer between Cr and Fe, and Si atoms above the dashed line is more pronounced than that observed with Ti and V replacing Fe atoms. The interaction between atoms above and below the dashed line is relatively strong. The situation in Fig. 7(a5)–(a7) is similar, and substituting Fe with Mo resulted in stronger interactions. In APB_{II}, after replacing Fe atoms with Cr, Nb, and Mo (Fig. 7(b4), (b6) and (b7)), compared with other elements replacing Fe atoms (Fig. 7(b2), (b3) and (b5)), the charge transfer between the neighboring atoms far above the dashed line is greater, and the interaction between atoms is stronger.

3.4.3. Bader charge. The Bader charge calculation results of atoms near the two types of anti-phase boundaries are shown in Fig. 8. A positive charge indicates the acquisition of electrons, while a negative charge indicates the loss of electrons. The replaced Fe atoms and doped atoms are considered the central atoms (CP atoms). The two atoms closest to the CP atoms above APB_I are Si and Fe (Fig. 8(a)), respectively. After sliding, the two atoms above APB_{II} become two Fe atoms (Fig. 8(b)). After doping, all alloy elements lose electrons, and the doping atoms near APB_{II} lose more electrons. Near APB_I (Fig. 8(a)), Si is an electron donor. After sliding (Fig. 8(b)), the original position of Si changes to Fe, and except for Ti and Zr doping, the originally lost electrons become gained electrons. In APB_{II} (Fig. 8(b)), the difference in charge transfer between the two atoms above is smaller than the difference in charge transfer between the two atoms above APB_I (Fig. 8(a)). The difference in the interaction between the two atoms above APB_{II} and the doped atom is also smaller.

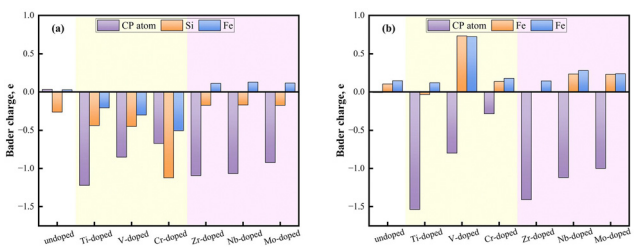

Fig. 8 Bader charge of atoms near the anti-phase boundaries, (a) APB_I; (b) APB_{II}.

4. Conclusions

The effects of alloying elements on two types of APBs, mechanical properties, and magnetic moments of $D0_3$ ordered structures in high silicon steel were studied through first-principles calculations. The following conclusions can be drawn.

APB_{II} has lower energy and is more sensitive to doping elements than APB_I. Among the six elements, Cr, Nb, and Mo elements, especially Cr and Mo elements, can reduce γ_{APB}. They also have a good effect on the plasticity of the $D0_3$ compounds based on the mechanical constants, giving a new explanation for the plasticizing mechanism of Cr and Nb. Adding Mo is theoretically feasible for high silicon steel.

The doping of alloying elements not only changes the local magnetic moment of Fe_I atoms and the interatomic interactions

but also introduces more unpaired electrons into the d-band of the compound, thus affecting the total magnetic moment of the compound.

The calculated charge density difference maps indicate that the charge transfer is stronger between the atoms across APB_{II} compared to APB_{I}, resulting in lower energy. Substituting Fe atoms with doping elements increases the charge transfer between atoms near APBs, thereby enhancing their interaction.

Author contributions

Conceptualization: Meng Sun, Hongyu Song, Shuai Tang, and Guichang Shen. Data curation: Meng Sun, Linxian Li, and Guichang Shen. Formal analysis: Meng Sun, Hongyu Song, Shuai Tang, and Guichang Shen. Funding acquisition: Shuai Tang and Qing Peng. Investigation: Meng Sun, Hongyu Song, Shuai Tang, and Fengliang Tan. Methodology: Meng Sun, Shuai Tang, Guichang Shen, and Tianwei Xie. Visualization: Meng Sun, Hongyu Song, Shuai Tang, and Guichang Shen. Supervision: Shuai Tang, Qing Peng, and Zhenyu Liu. Writing – original draft: Meng Sun. Writing – review and editing: Shuai Tang and Qing Peng.

Data availability

The data are available from the corresponding author on reasonable request.

Conflicts of interest

There are no conflicts to declare.

Acknowledgements

S. T. gratefully acknowledges the financial support of NSFC (No. 52175293 and 51774083), Q. P. would like to acknowledge the support provided by NSFC (No. 12272378) and Open Research Fund of State Key Laboratory of Rolling and Automation, Northeastern University (2022RALKFKT006).

References

1 G. Y. Ouyang, X. Chen, Y. F. Liang, C. Macziewski and J. Cui, *J. Magn. Magn. Mater.*, 2019, **481**, 234–250.
2 G. Y. Ouyang, C. R. Macziewski, B. Jensen, T. Ma, R. Choudhary, K. Dennis, L. Zhou, D. Paudyal, I. Anderson, M. J. Kramer and J. Cui, *Acta Mater.*, 2021, **205**, 116575.
3 X. L. Wang, Z. Y. Liu, H. Z. Li and G. D. Wang, *J. Magn. Magn. Mater.*, 2017, **433**, 8–16.
4 Y. F. Liang, F. Ye, J. P. Lin, Y. L. Wang and G. L. Chen, *J. Alloys Compd.*, 2010, **491**, 268–270.
5 A. M. Glezer, I. V. Maleeva and A. I. Zakharov, *Met. Sci. Heat Treat.*, 1985, **27**, 908–912.
6 F. González and Y. Houbaert, *Rev. Metal.*, 1988, **49**, 178–199.
7 C. Y. Han, F. Ye, H. Y. Du, B. B. Liu, Y. F. Liang, H. Li and H. L. Li, *Mater. Sci. Eng. A*, 2022, **851**, 143639.
8 W. M. Mao and P. Yang, *Sci. China: Technol. Sci.*, 2012, **55**, 2920–2925.
9 G. J. Cai, C. S. Li, B. Cai and Q. W. Wang, *Mater. Lett.*, 2019, **238**, 249–253.
10 K. Raviprasad and K. Chattopadhyay, *Mater. Sci. Eng.*, 1988, **98**, 281–284.
11 J. H. Yu, J. S. Shin, J. S. Bae, Z. H. Lee, T. D. Lee, H. M. Lee and E. J. Lavernia, *Mater. Sci. Eng. A*, 2001, **307**, 29–34.
12 W. S. Chen, J. Liu, Z. Y. Cheng, X. F. Lin and J. C. Zhu, *Mater. Today: Proc.*, 2015, **2S**, S314–S318.
13 J. B. Yu, H. Feng, S. Y. Jiang, L. F. Wang, P. Lin, D. Sun, B. Y. Yan and Y. Q. Zhang, *Mater. Charact.*, 2023, **204**, 113223.
14 G. T. Lin, F. Zhao, Z. H. Zhang and J. X. Xie, *Steel Res. Int.*, 2023, **94**, 2200463.
15 Z. Y. Cheng, J. Liu, Z. D. Xiang, J. Jia and Y. J. Bi, *Intermetallics*, 2020, **120**, 106747.
16 Z. Y. Cheng, J. Liu, W. S. Chen, J. C. Zhu, X. F. Lin and Z. D. Xiang, *J. Iron Steel Res. Int.*, 2016, **23**, 717–721.
17 I. N. Bakst, H. Yu, M. Bahadori, H. B. Yu, S. W. Lee, M. Aindow and C. R. Weinberger, *Int. J. Plast.*, 2018, **110**, 57–73.
18 K. Yoshimi, H. Terashima and S. Hanada, *Mater. Sci. Eng. A*, 1995, **194**, 53–61.
19 Y. L. Guo, B. Liu, W. Xie, Q. Lou and Q. Li, *Scr. Mater.*, 2021, **193**, 127–131.
20 H. Gholizadeh and S. Hasani, *Comput. Mater. Sci.*, 2018, **143**, 515–527.
21 Y. L. Li and W. J. Qiang, *Comput. Mater. Sci.*, 2022, **202**, 111005.
22 Y. L. Li and W. J. Qiang, *Mater. Chem. Phys.*, 2024, **311**, 128549.
23 Z. Y. Cheng, Z. X. Peng, B. L. Zhong, H. J. Liu, Z. H. Lu, S. C. Zhu and J. Liu, *Intermetallics*, 2023, **160**, 107918.
24 R. S. Sundar and S. C. Deevi, *Int. Mater. Rev.*, 2005, **50**, 157–192.
25 Y. L. Li, D. B. Yang and W. J. Qiang, *J. Magn. Magn. Mater.*, 2022, **562**, 169767.
26 F. Mao, H. Lu, F. W. Tang, K. Guo, D. Liu and X. Y. Song, *Acta Metall. Sin.*, 2021, **57**, 948–958.
27 C. G. McKamey, J. A. Horton and C. T. Liu, *J. Mater. Res.*, 1989, **4**, 1156–1163.
28 H. Y. Yasuda and Y. Umakoshi, *Intermetallics*, 2010, **18**, 1273–1278.
29 W. Y. Wang, F. Xue, Y. Zhang, S. L. Shang, Y. Wang, K. A. Darling, L. J. Kecskes, J. Li, X. Hui, Q. Feng and Z. K. Liu, *Acta Mater.*, 2018, **145**, 30–40.
30 G. Kresse and J. Furthmüller, *Comput. Mater. Sci.*, 1996, **6**, 15–50.
31 G. Kresse and J. Furthmüller, *Phys. Rev. B: Condens. Matter Mater. Phys.*, 1996, **54**, 11169–11186.
32 J. P. Perdew, J. A. Chevary and S. H. Vosko, *Phys. Rev. B: Condens. Matter Mater. Phys.*, 1993, **48**, 4978.
33 J. P. Perdew, K. Burke and M. Ernzerhof, *Phys. Rev. Lett.*, 1996, **77**, 3865–3868.
34 H. Z. Luo, Z. Y. Zhu, L. Ma, S. F. Xu, H. Y. Liu, J. P. Qu, Y. X. Li and G. H. Wu, *J. Phys. D Appl. Phys.*, 2007, **40**, 7121–7127.
35 J. F. Piamba, C. Ortega, R. Hernández-Bravo, J. M. González Carmona, J. A. Tabares, G. A. Pérez Alcázar and J. M. Alvarado-Orozco, *Appl. Phys. A*, 2020, **126**, 849.

36 O. I. Gorbatov, A. R. Kuznetsov, Y. N. Gornostyrev, A. V. Ruban, N. V. Ershov, V. A. Lukshina, Yu. P. Chernenkov and V. I. Fedorov, *J. Exp. Theor. Phys.*, 2011, **112**, 848–859.
37 K. Momma and F. Izumi, *J. Appl. Crystallogr.*, 2008, **41**, 653–658.
38 K. Momma and F. Izumi, *J. Appl. Crystallogr.*, 2011, **44**, 1272–1276.
39 Z. Q. Sun, W. Y. Yang, L. Z. Shen, Y. D. Huang, B. S. Zhang and J. L. Yang, *Mater. Sci. Eng. A*, 1998, **258**, 69–74.
40 T. J. Burch, J. I. Budnick, V. A. Niculescu, K. Raj and T. Litrenta, *Phys. Rev. B: Condens. Matter Mater. Phys.*, 1981, **24**, 3866–3883.
41 S. Pickart, T. Literenta, T. Burch and J. I. Budnick, *Phys. Lett.*, 1975, **53A**, 321–323.
42 C. Blaauw, G. R. MacKay and W. Leiper, *Solid State Commun.*, 1976, **18**, 729–730.
43 C. S. Li, G. J. Cai, B. Cai and Q. W. Wang, *J. Mater. Res.*, 2016, **31**, 3004–3015.
44 Q. D. Zhang, G. Huang and S. Li, *Crystals*, 2020, **10**, 488.
45 M. Born, K. Huang and M. Lax, *Am. J. Phys.*, 1955, **7**, 474.
46 A. Saengdeejing, Y. Chen, K. Suzuki, H. Miura and T. Mohri, *Comput. Mater. Sci.*, 2013, **70**, 100–106.
47 S. F. Pugh, XCII, *London, Edinburgh Dublin Philos. Mag. J. Sci.*, 1954, **45**, 823–843.
48 M. Pugaczowa-Michalska, A. Go, L. Dobrzyński and S. Lipiński, *J. Magn. Magn. Mater.*, 2003, **256**, 46–53.
49 R. Ma, Q. Xie, J. Huang, W. Y. Yan and X. T. Guo, *J. Alloys Compd.*, 2013, **552**, 324–328.
50 R. Ma, Q. Xie and J. Huang, *Intermetallics*, 2014, **46**, 12–17.